

1 **Fracture distribution on the Swift Reservoir Anticline, Montana: implications for structural and**
2 **lithological controls on fracture intensity**

3
4 Hannah Watkins^{1*}, Clare E. Bond¹, Adam J. Cawood¹, Mark A. Cooper¹² & Marian J. Warren³

5
6 ¹School of Geosciences, Meston Building, University of Aberdeen, Aberdeen, UK, AB24 3UE.

7 ²Sherwood GeoConsulting Inc., Suite 304, 1235 17th Ave SW, Calgary, Alberta, T2T 0C2, Canada.

8 ³Jenner GeoConsulting Inc., Suite 304, 1235 17th Ave SW, Calgary, Alberta, T2T 0C2, Canada.

9 *Correspondence (h.watkins@abdn.ac.uk)

10
11 **Abstract**

12 Where primary porosity and permeability of a rock are unfavourable for hydrocarbon production,
13 fractures can improve reservoir potential by enhancing permeability. Higher fracture intensity may
14 create a better connected fracture network, improving fractured reservoir quality. Investigations into
15 the controls on fracture intensity commonly conclude that either structural or lithological factors have
16 the greatest influence on fracture abundance. We use the Swift Reservoir Anticline in north western
17 Montana to investigate how fracture intensity varies throughout the structure, and determine that
18 although structural factors do influence fracture intensity, lithology is the main control at outcrop.

19 The Swift Reservoir Anticline exposes bedding surfaces of the Mississippian Castle Reef Formation
20 dolomite. Field data indicates that fracture intensity is highest in the fold forelimb, decreasing into the
21 backlimb except in outcrops of coarse dolomite where fracture intensity is low, regardless of structural
22 position. Field fracture intensity correlates with whole rock quartz, kaolinite and porosity percentages.
23 We suggest porosity and composition influence bulk rock mechanical properties, which, in turn,
24 control the fracture intensity at outcrop. Fracture intensity has a stronger relationship with lithological
25 than structural factors, therefore we suggest that the key to predicting fracture intensity in the
26 subsurface here is understanding how lithology varies spatially.

27
28 **Introduction**

29 Fractured reservoirs host hydrocarbon reserves globally, and are particularly beneficial to petroleum
30 systems with little primary porosity and permeability. Fractured reservoirs are productive from a wide
31 range of lithologies, from sedimentary rocks such as the tight sandstones of Bolivia (Florez-Niño et al.,
32 2005; Iñigo et al., 2012; Heidmann et al., 2017), to basement rocks such as the fractured granites of
33 Vietnam (Cuong & Warren, 2009). These reservoirs are found in a range of geological settings, from
34 relatively undeformed regions, where fractures form in response to regional stresses or increased
35 pore pressure (e.g. Engelder & Lacazette, 1990; Lacazette & Engelder, 1992), to tectonically deformed
36 regions, where stress concentrations have formed tectonic fractures on folds and around faults.
37 Fractured reservoirs form a significant contribution to global oil and gas reserves. For example the
38 Zagros fold-thrust belt, where oil and gas are produced primarily from the fractured Asmari Formation
39 carbonates, is one of the most prolific onshore regions of hydrocarbon exploration and production. It

40 has been estimated that this region alone contains 49 % of the global fold-thrust belt reserves (Cooper,
41 2007).

42 The contribution of fracture networks to the petroleum system varies depending on several fracture
43 attributes. Wider fracture apertures increase the secondary porosity and permeability, increasing fluid
44 flow (Odling et al., 1999); longer fractures increase the likelihood of fracture intersection, and
45 therefore can improve fracture network connectivity. Fracture network orientations play a role in
46 influencing fluid flow; orthogonal fracture sets are likely to intersect, improving fracture connectivity
47 and increasing the size of the effective fracture network (see Watkins et al., 2015a). The intensity of
48 fracture networks can also control fluid flow; higher fracture intensities (the total fracture length, area
49 or volume within a given area or volume) correlate with higher fracture connectivity (e.g. Watkins et
50 al., 2018); if a fracture network is well connected, fluids are able to migrate through the fractures
51 more easily. The controls on the spatial distribution of fracture network intensity is not fully
52 understood. A better understanding of the controls on fracture intensity distribution would allow
53 better prediction of the highest quality fractured reservoirs in the subsurface, and therefore better
54 targeting of these permeability sweet spots when drilling for oil and gas.

55 Current understanding of the controls on fracture intensity variation is often derived from outcrops
56 used as analogues to subsurface fractured reservoirs. These studies suggest that both structural and
57 lithological controls influence fracture intensity (e.g. Fischer & Jackson, 1999). Examples from a range
58 of sedimentary lithologies include studies that attribute fracture intensity variation to bed thickness
59 changes (e.g. Hobbs, 1967; Gross et al., 1995; Wennberg et al., 2007; Ortega et al., 2010; Barbier et
60 al., 2012), composition (e.g. McQuillan, 1973; Hugman & Friedman, 1979; Corbett et al., 1987; Hanks
61 et al., 1997; Ferrill & Morris, 2008), grain size (e.g. Hanks et al., 1997; Nelson, 2001; Wennberg et al.,
62 2007), porosity (e.g. Corbett et al., 1987; Barbier et al., 2012), 'degree of tectonic deformation' (e.g.
63 Hobbs, 1967), structural position on a fold (e.g. Hanks et al., 1997; Wennberg et al., 2007), proximity
64 to faults (e.g. Hanks et al., 1997), and bedding curvature (e.g. Ramsay, 1967; Lisle, 1992; Lisle, 1994;
65 Ortega et al., 2010). The question is, in a geological setting where any number of these variables
66 change, which are the dominant factors that control fracturing?

67 Evidence for structure and lithology controlling fracture intensity are well reported in the literature
68 (see previous paragraph); we aim to add to this knowledge base, assessing the relative contribution
69 of lithological and structural controls on fracture formation using an anticline of dolomite in the
70 Sawtooth Range of Montana, USA. Using field data we separately assess how structural (simple
71 curvature and bedding dip) and lithological (grain size, porosity, composition) factors correlate to
72 fracture intensity variation, and we use results from this analysis to discuss which has the greatest
73 influence on fracture formation.

74

75 **Sawtooth Range**

76 *Regional Geology*

77 We use an anticline in the Sawtooth Range of Montana, USA, to analyse fractures. The Sawtooth Range
78 is an arcuate fold-thrust belt formed in the Palaeocene (Mudge, 1982) during the Cordilleran Orogeny
79 (Fuentes et al., 2012). It is located on the eastern edge of the Rocky Mountains in north-west Montana,
80 bounded to the east by the Mesozoic-Palaeogene foreland basin, and to the west by the Lewis and
81 Eldorado Thrust system, which separates Proterozoic-Palaeozoic rocks in its hangingwall from
82 Palaeozoic-Mesozoic rocks in its footwall (Figure 1). The Sawtooth Range is in the footwall to the

83 Lewis-Eldorado Thrust system, and has been interpreted by many authors to be a thin-skinned fold-
84 thrust belt (Mudge, 1982; Mitra, 1986; Holl & Anastasio, 1992; Fuentes et al., 2012).

85 The Sawtooth Range has been chosen for this study to represent an along-strike equivalent to the
86 subsurface fractured reservoirs in the Front Ranges of Alberta. Here, most hydrocarbons are produced
87 from Carboniferous carbonates similar to those exposed in the Sawtooth Range; some intervals rely
88 on fracture permeability for commercial production (e.g. Rawnsley et al., 2007). The Alberta Foothills
89 reservoir equivalent intervals and trap geometries, however, are not well exposed at outcrop. In
90 contrast, equivalent carbonates and anticlinal trap geometries can be observed on well-exposed
91 outcrop in the Sawtooth Range, and as such they make good outcrop analogues to study the causes
92 behind variation in fracture networks. For this study we focus on one anticline, namely the Swift
93 Reservoir Anticline. The present erosion level exposes extensive areas of bedding surfaces associated
94 with several depositional cycles near and at the top of the Mississippian. All observed bedding surfaces
95 on the Swift Reservoir Anticline are heavily fractured, so the spatial distribution of fracture intensity
96 variation in 2D can be studied. However, for the outcrops studied only the top surface of beds can be
97 observed, meaning fracture network variation in 3D cannot be studied, nor can the control of
98 mechanical layer/bedding thickness on fracture intensity. In this study we aim to determine how
99 structural controls relating to the geometry of the fold, as well as lithology, influence fracture intensity
100 by analysing fracture data from various structural positions, and from the tops of different beds with
101 different lithological properties.

102 *Structural, Burial and Regional Stress History*

103 NW Montana and adjacent SW Alberta record a complex tectonic and depositional history from
104 PreCambrian to Cenozoic time (e.g. Mudge, 1982; Price, 1994; Fuentes et al., 2012). We only address
105 here components potentially relevant to burial history and brittle deformation of the Lower
106 Mississippian rocks observed at Swift Reservoir Anticline. Lower Mississippian rocks were deposited
107 on a continental margin most commonly interpreted as an eastward-tapering marine foreland or back-
108 arc basin that developed in response to convergent plate motion to the west. Early Mississippian
109 deposition was influenced by local margin-parallel extensional faults perhaps related to foreland basin
110 flexural processes or back arc extension, and by reactivation of pre-existing structures oblique to the
111 margin (Reid and Dorobek, 1993; Batt et al., 2008; Cooley et al., 2011). A significant Carboniferous to
112 Jurassic unconformity in the Sawtooth Range records widespread non-deposition and/or erosion in
113 NW Montana and SW Alberta, during complex, ongoing convergent plate interactions to the west.
114 Much of this unconformity is perhaps associated with passage of a Jurassic flexural forebulge prior to
115 local thrusting, driven by a period of terrane accretion and thrusting to the west (Ward and Sears,
116 2007; Fuentes et al., 2011). This unconformity is well exposed on Swift Reservoir Anticline (Mudge,
117 1982; Ward & Sears, 2007). Therefore the pre-Cretaceous tectonic history implies possibly complex
118 perturbations in stress regime with related brittle deformation during and following deposition, but
119 before compressional folding. Pre-Jurassic deformation at Swift Reservoir is addressed in more detail
120 below.

121 By Middle Jurassic time, a north-eastward propagating fold-thrust belt developed on the former
122 continental margin, accompanied by widespread subsidence and clastic fill of an associated foreland
123 basin to the east. Fold-thrust deformation, including the Swift Reservoir Anticline, involved the
124 Paleozoic carbonate and Mesozoic clastic rocks of the Sawtooth Range by latest Cretaceous to
125 Paleocene time (Fuentes et al., 2012).

126 Extension occurred in NW Montana during the mid-Eocene to Oligocene (Constenius, 1996; Fuentes
127 et al., 2011) in association with regional, crustal-scale extension in the hinterland parts of the thrust

128 belt (Price, 1994). There is little or no stratigraphic record or clear structural evidence for extensional
129 deformation in the Montana Sawtooth Range or correlative southern Alberta Foothills; however,
130 Eocene to Oligocene syn-extensional clastic deposits are locally exposed in extensional fault
131 hangingwalls to the northwest of the Sawtooth Range (McMannis, 1965; Constenius, 1996; Figure 1).
132 Therefore we cannot rule out the possibility that the extensional event contributed to fractures
133 observed at Swift Reservoir Anticline; there is however no direct evidence for this, and present-day
134 maximum horizontal stress orientations are consistently SW-NE as supported by abundant subsurface
135 data in central to southernmost Alberta (Bell and Babcock, 1986; Bell, 1994; Heidbach et al., 2008).

136 Burial data for subsurface Mississippian rocks in the eastern Foothills in southern Alberta indicate
137 increasing sedimentary and subsequent tectonic burial from the Jurassic to a maximum of close to 10
138 km in the Paleocene. This was followed by exhumation to their current depth of on the order of 5 km
139 (Price, 1994; Hardebol et al., 2009). In the Sawtooth Range equivalent rocks were probably buried
140 much less deeply before Cenozoic uplift and present exposure at surface. Quantitative data however
141 are limited to perhaps uncertain conodont colour alteration index analyses from the Mississippian
142 carbonate section that imply a maximum burial to no more than about 2-3 km (Nichols, 1986).

143 *Mississippian Stratigraphy*

144 Cyclicity and depositional thickness variations in the Lower Mississippian Castle Reef Formation
145 contribute directly to the mechanical heterogeneity of the carbonate succession and thus fracture
146 distribution at Swift Reservoir Anticline. The Lower to Middle Mississippian Madison Group contains
147 two main lithostratigraphic subdivisions in the Sawtooth Range (Mudge, 1962; Nichols, 1984): the
148 lower, dominantly limestone Allan Mountain Formation and the conformably overlying Castle Reef
149 Formation, comprising mainly bioclastic dolomites with both primary and secondary dolomitization.
150 The Castle Reef Formation has in turn been divided into a lower Gateway Pass Unit of crinoidal
151 grainstones and interbedded dolomitic mudstone/wackestone, grading upwards into a Dupuyer Creek
152 Unit of cyclically interbedded packstone, wackestone and mudstone, which is well exposed at Swift
153 Reservoir Anticline (Nichols, 1984). The Castle Reef Formation varies in thickness due to erosion
154 beneath the sub-Jurassic unconformity over the entire Sawtooth Range but averages 215 m in the
155 Swift Reservoir area (Singdahlsen, 1986), and the Dupuyer Creek Unit varies in thickness from 30-75
156 m.

157 The entire Mississippian succession in western Montana is interpreted (Reid and Dorobek, 1993; Batt
158 et al. 2007) to record overall a prograding carbonate ramp from deep water (Allan Mountain
159 Formation) through shallow high-energy conditions (Castle Reef Formation, Gateway Pass Unit) to a
160 tidally-influenced interior ramp setting (Castle Reef Formation, Dupuyer Creek Unit). Deposition in the
161 upper, low-accommodation part of the section is marked by higher-order sea-level fluctuations,
162 resulting in lithological cyclicity, on the order of 0.5 to 5 m, from mud-dominated to grain-dominated
163 facies in the Dupuyer Creek Unit where it is exposed at Swift Reservoir (Figure 2). The current erosion
164 surface across the Swift Reservoir Anticline exposes approximately 100 m of Castle Reef Fm. beneath
165 the unconformity, so it is likely that the coarser-grained facies at the lowest exposure levels are within
166 the upper part of the Gateway Pass Unit.

167 *Swift Reservoir Anticline*

168 The Swift Reservoir Anticline is on the north-eastern margin of the Sawtooth Range (Figure 1, Figure
169 3a), bounded to the west by structurally overlying fold-thrust structures and to the east by less
170 deformed Mesozoic rocks in the foothills and western foreland basin (Figure 3d). The Swift Reservoir
171 Anticline exposes folded Mississippian Castle Reef Formation dolomites, which form a strongly

172 asymmetric fold structure (Figure 3b, 3d). The fold has a steep forelimb dipping to the northeast, and
173 shallow backlimb dipping to the southwest. The thrust relationships in this part of the Sawtooth Range
174 are very complex and are best illustrated by the detailed surface maps of Ross (2016), north of Swift
175 Reservoir, and Singdahlsen (1986), south of Swift Reservoir. These maps have been used together with
176 data collected during this project to create the cross-section through the Swift Reservoir Anticline
177 (Figure 3d). An additional critical data constraint for the structural model is the Blackfeet Tribal 12-1
178 well. The well data publicly available from the Montana Bureau of Mines and Geology is limited to the
179 location, total depth and the depths of the three penetrations of the top of the Mississippian, but
180 Singdahlsen (1986; cross-section A-A') indicates that he had access to additional significant
181 stratigraphic detail in the well.

182 The Blackfeet Tribal 12-1 well is located on the outcropping Cambrian sediments in the hangingwall
183 of the Major Steel Backbone Thrust (MSBT). The well penetrates the underlying thrust sheet that
184 includes the Swift Reservoir Anticline, and it intersects the Swift Thrust close to the base of the
185 Mississippian section. In the footwall of the Swift Thrust, a structurally thickened package of the
186 Cretaceous Kootenai Fm correlates up-dip to surface to the Eagle Creek Imbricate Zone (ECIZ)
187 (Singdahlsen, 1986) with a floor thrust, the Fish Lake Thrust (FLT), located close to the base of the
188 younger Cretaceous Blackleaf Fm. Beneath this floor thrust, a conformable sequence from the
189 Blackleaf Fm to the base of the Mississippian is carried by the deepest thrust in the system, the Old
190 Man Thrust (OMT). The Mississippian in the hangingwall of the OMT outcrops to the south (Berg, 2002
191 and Singdahlsen, 1986), confirming the subsurface geometry implied by the well. The well penetrates
192 the OMT with Cretaceous Kootenai Fm in the footwall, and ultimately terminates in the upper
193 Mississippian which is apparently at regional elevation and likely unthrust.

194 Although the model is well constrained by surface and subsurface data, uncertainty remains for the
195 evolution of the Swift Reservoir Anticline, mostly due to out-of-sequence thrusting. The OMT thrust
196 sheet when restored would contain at its western end the footwall ramp cut-off that matches the
197 hangingwall cut-off represented by the forelimb of the Swift Anticline. This is not shown on the cross
198 section (Figure 3d) because the MSBT appears to be out-of-sequence, truncating two thrust repeats
199 of Mississippian stratigraphy in its footwall. The OMT folds the FLT and likely folds the Swift Thrust as
200 well. The OMT, close to the hangingwall cut-off of the Mississippian, is imbricated by a couple of thrust
201 splays one of which comes to surface very close to the FLT. Another splay is mapped as the Mitten
202 Lake Thrust (MLT). The final splay is the most external thrust mapped which is not named but is
203 labelled as A on the cross section (Figure 3d). It is therefore difficult to determine the kinematic history
204 of the Swift Reservoir Anticline given the structural complexity described above, particularly the lack
205 of a matching footwall counterpart to the anticline. A suggested model of early development,
206 however, is shown in Figure 3e. This model proposes an early history as a fault propagation fold,
207 perhaps combined with trishear type strain ahead of the propagating fault tip, which would result in
208 the tight fold hinge and steep to vertical or locally overturned forelimb.

209 To study how the fracture network varies on the Swift Reservoir Anticline, first we need to be sure
210 that the fractures observed at outcrop might relate to the Late Cretaceous-Palaeocene compressional
211 folding process rather than another earlier or later phase of deformation. Karst-widened fractures
212 associated with the Carboniferous-Jurassic uplift can be found in the Castle Reef Formation dolomite
213 at Swift Reservoir (Ward & Sears, 2007). These fractures penetrate the Castle Reef Formation for up
214 to 4 m beneath the unconformity surface, and are filled with cherty sandstone and conglomerate from
215 the base of the Jurassic (Ward, 2007; Ward & Sears, 2007). However we only observed evidence for
216 these fractures in the fold forelimb at the northern end of the structure close to the preserved
217 unconformity surface; elsewhere no evidence for karstified fractures could be seen. The outcrops

218 containing the karstified fractures also contain narrow aperture, non-karstified joint sets that are alike
219 in attributes to the rest of the fractures that we sampled throughout the fold. These narrow fractures
220 cut across the sand and conglomerate fill in the karstified fractures so are clearly younger. It is these
221 narrow, younger fractures that we have sampled in this study; although older fracture sets are present
222 in the structure, they are easily distinguished in the field due to their sand/conglomerate fill, and have
223 been excluded from this study.

224

225 **Methods**

226 *Fieldwork*

227 To assess both the structural and lithological controls of fracture intensity on the Swift Reservoir
228 Anticline we collected data in the field from eleven transects oriented normal to the fold hinge along
229 a 2 km segment of the fold (Figure 4). The lengths of individual transects ranged from 145-560 m and
230 the spacing between transects ranged from 95-430 m, depending on outcrop availability. Field data
231 was collected from a total of 193 sampling sites, which were located along transects in fold backlimb,
232 hinge and forelimb positions. At each sampling site the bedding dip was measured, a scaled and
233 oriented photograph was taken orthogonal to bedding, and the lithology was recorded. All sampling
234 sites are located in the Castle Reef Formation dolomite; lithology was classified depending on the grain
235 content of the rock. Sampling sites were allocated one of three lithological classifications: 1) Grain
236 Supported Dolomite (GSD); coarse dolomite (grainstone) with shell and coral fragments, 2) Mud
237 Supported Dolomite (MSD); fine grained dolomite (mudstone) lacking clear grains and an intermediate
238 phase of 3) Mud/Grain Supported Dolomite (MGSD); fine grained dolomite (wackestone-packestone)
239 with identifiable grains and small shell fragments. Variations in lithology are attributed to sampling
240 sites being located on different bedding surfaces (i.e. from different stratigraphic horizons in the Castle
241 Reef Formation). As well as classifying lithology in the field, hand specimens from 10 of the sampling
242 sites (5 GSD & 5 MSD) were collected for further analysis (see Figure 4 for hand specimen locations).

243 *Fracture intensity estimation*

244 Fracture (joint) intensity was estimated for each sampling site using digital circular scanlines. Bedding
245 surface photographs taken at each sampling site were scaled and oriented using Move software. A
246 digital circle of known radius was placed on the photograph and the number of intersections with this
247 circle was recorded. The fracture intensity for each sampling site was estimated using Mauldon's
248 circular scanline method:

$$249 \quad I = n/(4r)$$

250 I = estimated fracture intensity (m/m^2), n = number of fracture intersections with the digital circle, and
251 r = circle radius (m) (Mauldon et al., 2001). Estimated fracture intensity is given as fracture length per
252 unit area on the bedding surface. Sampling circle radii ranged from 8-39 cm; the exact size of the circle
253 was chosen to attain a minimum n value of 30, as suggested by Rohrbaugh et al. (2002). Circular
254 scanline sampling was chosen because it does not incur any orientation bias, and therefore no
255 orientation correction is required. Although the circular scanline method only estimates fracture
256 intensity it has been tested against other data collection methods that record the actual fracture
257 intensity at outcrop, such as areal sampling (Watkins et al., 2015b), and has been shown to produce
258 accurate results.

259 *Lithological analysis*

260 From the 10 hand specimens oriented thin sections for each were cut normal to bedding and parallel
261 to the bedding dip direction. SEM (Scanning Electron Microscope) analysis was used to analyse thin
262 sections using Back Scatter Electron (BSE) imaging. 12-15 randomly selected images of each thin
263 section were collected for further image analysis using ImageJ software. In ImageJ, the percentages of
264 lithological properties (porosity, dolomite, quartz, calcite, kaolinite, other mineral) were calculated for
265 each image using the following workflow: 1) set image scale, 2) adjust image brightness and contrast
266 until the lithological property of interest is shown in black, and the rest of the image is shown in white,
267 3) 'despeckle' the image to remove noise, 4) convert image to binary, 5) analyse the binary image to
268 determine the percentage area of the lithological property of interest.

269 *3D model building & predictions*

270 Pseudosurfaces for the top Castle Reef Formation and fifteen arbitrary horizons beneath were
271 constructed using Move software to extract curvature data from. These surfaces were built to
272 represent the large scale fold geometry rather than the actual top Castle Reef Formation, which may,
273 in reality, not be a single horizon surface. Cross sections for the Top Castle Reef Formation were
274 constructed for each transect using field bedding data and geological map boundaries (Mudge &
275 Earhart, 1983). A 3D surface for this horizon was then constructed using a spline curves algorithm; the
276 resultant surface was analysed using curvature analysis to determine non-geological anomalies on the
277 surface geometry. The cross sections were adjusted to remove anomalies, whilst ensuring the top
278 Castle Reef Formation horizon geometry still adhered to field data. The 3D surface was reconstructed
279 and resampled to make a mesh surface made up of individual triangular segments whose edge lengths
280 measured no more than 20 m. In addition to this 15 more surfaces were created below the top Castle
281 Reef Formation horizon, using lines constructed parallel to the original Castle Reef Formation horizon
282 on each cross section. These arbitrary surfaces were spaced at 10 m intervals, parallel to the top Castle
283 Reef Formation surface above. Field sampling site localities were then projected to the nearest 3D
284 surface, and a value for simple curvature for each sampling site was extracted from the 3D surfaces.

285 Figure 5 shows the 3D surface for the top Castle Reef Formation horizon, colour mapped for simple
286 curvature, which is the rate of change of dip measured in the direction of maximum dip (e.g. Hennings
287 et al., 2000). The 3D model shows a narrow, high curvature fold forelimb and much lower curvature
288 in the hinge zone and fold backlimb. Curvature in the fold backlimb is consistently low throughout the
289 entire structure, curvature in the hinge zone increases slightly to the SE, and the fold forelimb
290 curvature is much higher in the NW compared to elsewhere along strike. In theory surfaces with higher
291 curvature have undergone more strain to attain those geometries, although in practice this is not
292 always the case (e.g. Chester et al., 1991; Hedlund et al., 1994; Lemiszki et al., 1994; Salvini and Storti
293 2001; Tavani et al., 2015) so we would predict from our model that fracture intensity should be highest
294 at the northeastern end of the fold forelimb where fold curvature is highest (Figure 5), decreasing
295 along strike. Fracture intensity in the hinge zone and fold backlimb are predicted to be very low in
296 comparison to the fold forelimb due to lower curvatures, but may increase slightly to the south-east,
297 where curvature is slightly elevated. We test these predictions using our field data.

298

299 **Results**

300 Fractures observed on bedding surfaces are predominantly interpreted to be joints, having very few
301 observable offsets. Fractures tend to be very narrow (<1 mm aperture) and are mostly open. The
302 orientations of all measured fractures are presented as a rose plot on Figure 4. In total the orientations
303 of 24744 fractures were measured, inherently producing significant data scatter when presented on

304 a single rose plot. It is, however possible to distinguish two dominant fracture set orientations; one
305 being oriented NW-SE, parallel to the fold hinge (i.e. Price's (1966) J1 fractures); and a second aligning
306 NE-SW, normal to the fold hinge (i.e. Price's (1966) J2 fractures). These orientation distributions reflect
307 the data from individual sampling sites, where two dominant sets are usually present, aligning normal
308 and parallel to the fold hinge. The orientations of these two fracture sets varies throughout the fold,
309 but may be due to changes in the orientation of the fold hinge along strike (see Figure 4).

310 Fracture intensity estimations are presented on Figure 4; estimations range from 23 to 464 m/m².
311 From initial observation of the fracture intensity distribution no clear pattern is observed. Estimated
312 fracture intensity is highest in the fold forelimb at the northern end of the structure, where simple
313 curvature is highest (Figure 5); elsewhere fracture intensity distribution appears almost random. To
314 understand the controls on fracture intensity we analyse structural and lithological factors separately.

315 *Fracture intensity: structural controls*

316 Scatter graphs for fracture intensity versus simple curvature and bedding dip for all sampling sites are
317 shown on Figure 6. Due to the nature of exposure on the Swift Reservoir Anticline the majority of our
318 data points are from MSD lithologies (blue, n = 153); with only a small number of sampling sites located
319 on MGSD (yellow, n = 16) and GSD (red, n = 15) bedding surfaces. This means that trends in MSD
320 datasets are likely to be more statistically valid than those from MGSD and GSD datasets. For MSD
321 sampling sites both graphs (Figure 6a and 6b) show positive correlations, with fracture intensity
322 increasing with increasing simple curvature and bedding dip. However both graphs show significant
323 data scatter, resulting in only low-moderate correlation coefficients ($R^2 = 0.41$ Figure 6a; $R^2 = 0.30$,
324 Figure 6b). For MGSD and GSD datasets Figure 6a and 6b show poor correlation coefficients. Almost
325 no correlation between simple curvature and fracture intensity is observed from either dataset on
326 Figure 6a, and between bedding dip and fracture intensity for MGSD sampling sites on Figure 6b. A
327 weak negative correlation is observed between fracture intensity and bedding dip for GSD sampling
328 sites (Figure 6b). To further investigate how fracture intensity varies at different structural positions,
329 bar charts for the average fracture intensity in forelimb, hinge zone and backlimb positions were
330 plotted for each lithology (Figure 6c). The graph suggests the highest fracture intensities are found in
331 MSD's outcropping in the fold forelimb, decreasing into the hinge zone and backlimb. Little variation
332 in average fracture intensity in MGSD and GSD lithologies are observed at different structural
333 positions.

334 To understand the cause behind the data scatter on Figure 6a and 6b we focus on individual sampling
335 transects. Figure 7 shows how estimated fracture intensity varies with simple curvature, bedding dip
336 and structural position for transects 1 and 10 (see Figures 4 & 5 for transect locations). Transect 1
337 shows that estimated fracture intensity increases with both simple curvature and bedding dip (Figure
338 7a & 7b). The linear correlation coefficient for both graphs is 0.42, suggesting only moderate data
339 scatter. The cross section (Figure 7c) shows a gradual increase in fracture intensity from the fold
340 backlimb to the fold forelimb.

341 Scatter graphs for transect 10 show a negative correlation between estimated fracture intensity and
342 simple curvature (Figure 7d) and a positive correlation between estimated fracture intensity and
343 bedding dip (Figure 7e), suggesting a more complicated relationship between structural controls and
344 fracture intensity than indicated by transect 1. The cross section for transect 10 (Figure 7f) shows a
345 gradual decrease in fracture intensity from the fold backlimb to the fold forelimb. A notable difference
346 between transects 1 and 10 is that transect 1 is only sampled in a single lithology (MSD), whereas
347 transect 10 samples three lithologies (MSD, MGSD & GSD); this difference is due to differences in relief
348 and hence stratigraphic position on the two transects. Figures 7d & 7e show that data from each of

349 the three lithologies are clustered on the graphs, indicative of a lithological control on fracture
350 intensity.

351 *Fracture intensity: lithological controls*

352 *Field lithological classification*

353 Figure 8a shows how fracture intensity varies with lithology. GSD outcrops consistently show low
354 estimated fracture intensity (min: 27.00 m/m², median: 60.00 m/m², max: 89.00 m/m²), with low
355 standard deviation (21.97); MGSD outcrops show moderate estimated fracture intensity (min: 58.00
356 m/m², median: 139.38 m/m², max: 216.25 m/m²), but data points are scattered resulting in a higher
357 standard deviation (35.30) than for GSD. MSD outcrops exhibit higher estimated fracture intensities
358 than other lithologies (min: 60.83 m/m², median: 143.75 m/m², max: 463.33 m/m²) but data scatter
359 also means a high standard deviation (72.52). Average estimated fracture intensity for each of the
360 three lithologies (Figure 8b) clearly shows a relationship between fracture intensity and lithology;
361 average fracture intensity is highest in finer grained rocks and decreases as grain size increases. It
362 should be noted that, since the majority of the Swift Reservoir Anticline exposes the MSD lithology,
363 average values for fracture intensity have been calculated from a lower number of sampling sites for
364 MGSD and GSD.

365 *Thin section analysis*

366 The composition of 10 GSD and MSD hand specimens were determined using thin section analysis on
367 BSE (Back-Scatter Electron) images from an SEM (Scanning Electron Microscope) and image analysis,
368 using ImageJ software. Examples of three binary images for porosity, calcite and quartz distribution
369 for the thin section imaged in Figure 9e are shown in Figure 9a-9c. Analysis reveals GSD and MSD hand
370 specimens have quite different compositions, textures and porosities. Figure 9d and 9e show typical
371 BSE images of GSD lithologies; hand specimens are primarily composed of coarse/recrystallized
372 dolomite (average 90.12 %, Figure 9h) and pore space (average 8.60 %, Figure 9h). Minor components
373 of quartz (average 1.04 %, Figure 9h), accessory minerals (metal oxides, average 0.05 %, Figure 9h)
374 and secondary calcite found only in fractures or pore space are also seen (average 0.08 %, Figure 9h).
375 Figure 9f and 9g show typical BSE images of MSD lithologies; hand specimens are primarily composed
376 of fine grained dolomite (average 91.60 %, Figure 9h), pore space (average 4.14 %, Figure 9h) and
377 quartz (average 3.68 %, Figure 9h), with minor components of kaolinite (average 0.28 %, Figure 9h),
378 accessory minerals (average 0.23 %, Figure 9h) and calcite (average 0.15 %, Figure 9h).

379 Average percentages for the main mineral components and porosity were calculated for each hand
380 specimen and plotted against estimated fracture intensity (Figure 10) to investigate the role of
381 different lithological factors on fracture intensity. A negative correlation ($R^2 = 0.23$) is found between
382 estimated fracture intensity and porosity (Figure 10a); generally hand specimens with higher
383 estimated fracture intensity have low estimated porosity values, whereas most hand specimens with
384 low estimated fracture intensity have higher estimated porosity values. Estimated fracture intensity
385 shows almost no correlation with dolomite percentage ($R^2 = 0.03$) (Figure 10b), probably because the
386 dolomite percentage varies very little. A positive correlation between estimated fracture intensity and
387 quartz percentage is shown on Figure 10c ($R^2 = 0.39$). The graph shows that hand specimens with
388 higher quartz content generally have higher fracture intensity than those with lower quartz content.
389 A positive correlation is also seen between estimated fracture intensity and kaolinite content ($R^2 =$
390 0.39 , Figure 10d). Hand specimens with low kaolinite content tend to have low estimated fracture
391 intensity, whereas hand specimens with more kaolinite have higher estimated fracture intensities.
392 Figure 10e shows a moderate correlation ($R^2 = 0.15$) between estimated fracture intensity and calcite

393 percentage; however given that only three of our hand specimens contain calcite, and that most of
394 that calcite is observed in fractures/pores (Figure 9) suggests that it was probably was not present
395 during the main phase of fracturing, and therefore calcite is unlikely to have influenced fracture
396 intensity. A positive correlation is also seen between quartz and kaolinite content (Figure 10f); the
397 implications of this correlation will be considered in the discussion.

398

399 **Discussion**

400 *Structural versus lithological control on fracture intensity*

401 Correlation between fold simple curvature, bedding dip, and structural position with estimated
402 fracture intensity can be seen in our data (Figure 6). Estimated fracture intensity increases as simple
403 curvature and bedding dip increase, suggesting that these two factors are related to fracture
404 formation. These relationships are clearest where data is collected from a single lithology; for example
405 data from Transect 1 (Figure 7) is collected in only Mud-Supported Dolomites. Here positive linear
406 correlation coefficients for these variables are moderate (Figure 7a-c). Generally higher simple
407 curvatures and bedding dips are found in the fold forelimb, where fracture intensity is highest, and
408 they decrease south-westward into the fold backlimb, where fracture intensities are lowest (Figure
409 7a-c). When analysing the data in more detail we see that these relationships between structural
410 controls and estimated fracture intensity only hold true where lithology is consistent (e.g. Figure 7d-
411 f); our data shows that, regardless of structural position, fracture intensity will be higher in mud-
412 supported dolomites than grain-supported dolomites. This means that the high curvature, steeply
413 dipping fold forelimb, if sampled in a mud-supported dolomite fracture intensity will be high, whereas
414 in a grain-supported dolomite, fracture intensity will be lower (Figure 11).

415 Relationships between fold curvature and fracture intensity have been discussed at length in
416 published literature, and stem from work by Ramsay (1967), who proposed relationships between
417 strain and fold curvature in two dimensions. Lisle (1992; 1994) further developed work by Ramsay
418 (1967) by assessing how strain and curvature relate in three dimensions. Lisle uses curvature analysis
419 to detect zones high strain on folded surfaces, and suggests that this curvature analysis could be used
420 to predict the density of sub-seismic scale deformation such as fracturing (Lisle, 1994). Lisle (1994)
421 uses the theory that surfaces with double curvature (i.e. a non-cylindrical fold) must form with some
422 stretching or contraction of the bedding, meaning that the total curvature (product of the two
423 principle curvatures) is proportional to strain magnitude. This theory was tested by Lisle (1994) on the
424 Goose Egg Dome in Wyoming, where the highest fracture densities, measured by Harris et al., 1960,
425 were found in regions of highest total curvature. Other studies have used this predicted relationship
426 between curvature and strain/fracture intensity to predict fracture intensity on fold structures.
427 Hennings et al. (2000) use the rate of change of dip (i.e. simple curvature) on the Oil Mountain
428 Anticline in Wyoming to populate a 3D fold model with fracture intensity estimates based on the
429 assumption that fracture intensity increases with increasing curvature.

430 However, in many other investigations into the role of curvature and structural position in controlling
431 fracture intensity and density, it has been found that correlations are poor. Examples include Ortega
432 et al. (2010), whose suggest that only a moderate to weak correlation between fracture intensity and
433 fold curvature can be observed in carbonates of the Sierra Madre Oriental in northeast Mexico.
434 McQuillan (1973) uses outcrops from the Asmari Formation in the Zagros to determine that fracture
435 density is independent of structural position. Bergbauer & Pollard (2004) suggest that fracture
436 intensity is higher on sandstone folds than in between fold structures, however there is little variation

437 in fracture intensity within individual fold structures. Our study suggests that although fracture
438 intensity is influenced by structural factors such as bedding dip, fold curvature and structural position,
439 it is the lithology that is the main control on fracture intensity distribution across the fold structure.
440 The implications for this are that fracture intensity prediction in subsurface structures may be better
441 aided by determining how lithology changes spatially rather than focussing on characterising the
442 geometry of a fold and modelling its evolution.

443 Based on fracture orientations we classified our fracture sets as Price's (1966) hinge-parallel (J1) or
444 hinge-normal (J2) fractures that form in response to folding. An alternative model could be that the
445 fractures observed are in fact pre-folding joints associated with foreland flexuring in the peripheral
446 bulge region that are later tilted as the fold develops (Tavani et al., 2015). The elevation of fracture
447 intensity in the forelimb could then be caused by late - stage fold tightening that increases fracture
448 frequency in this region alone (i.e. backlimb and hinge-zone fractures are all pre-folding features). If
449 this is the case then folding-associated strains influence fracturing in the forelimb region alone, not
450 the backlimb and hinge zone regions. The resultant fracture sets for both models (pre-folding and fold-
451 associated fracturing) are likely to produce very similar fracture patterns (i.e. hinge-parallel and hinge-
452 normal joints perpendicular to bedding), so it is difficult to distinguish between them.

453

454 *Lithological control on fracture intensity*

455 Using image analysis of Back-Scatter Electron (BSE) photographs we were able to determine that
456 fracture intensity shows some correlation with the proportion of porosity, quartz and kaolinite (Figure
457 10). The reason for this probably relates to these lithological factors influencing overall rock strength.
458 It is thought that fracture intensity increases with increasing rock strength because stronger rocks
459 tend to be more brittle, so that when they fail they produce closely spaced, high density fracture
460 networks (Nelson, 2001). Our data suggests that fracture intensity increases with decreasing porosity
461 (Figure 10a); similar correlations have been observed elsewhere, for example Nelson (2001) reports
462 increasing fracture intensity with decreasing porosity in carbonates further south in the Sawtooth
463 Range. The negative correlation between fracture intensity and porosity observed in our study could
464 be explained by strain accommodation during deformation. One explanation might be that pore
465 spaces act as weak zones in the rock; as stress is applied to the rocks during folding, the pore space
466 may accommodate strain by distortion of the pore boundaries (i.e. elastic behaviour). Bounding grains
467 could be pushed into the pore space, accommodating a significant portion of the overall strain,
468 meaning only a limited number of fractures need to form to accommodate the remaining strain. In
469 rocks with very low porosity, such as the mud-supported dolomites in our study area, limited pore
470 space might mean very little pre-failure strain can be accommodated by pore space rearrangement
471 (elasticity) so instead a large number of fractures form. If this was the case we might expect to see
472 evidence for pore shape deformation. Although our BSE images of thin sections clearly show many
473 pores, we cannot assess the degree of pore shape deformation because we do not have any evidence
474 of the pore shapes prior to folding.

475 Compositional correlations with estimated fracture intensity are also observed from our data. Fracture
476 intensity increases with both increasing quartz and kaolinite content (Figure 10c, 10d). Quartz is a
477 strong, brittle mineral; increasing the amount of quartz in a rock will probably also increase the bulk
478 strength and brittleness of that rock. Based on Nelson's (2001) suggestion that rocks with a higher
479 percentage of brittle constituents will have closer spaced (and therefore higher intensity) fractures, it
480 would be expected that rocks with more quartz will have a higher fracture intensity than those with

481 less brittle constituents, which fits our data. The positive correlation between estimated fracture
482 intensity and kaolinite percentage is more puzzling. Kaolinite is a clay mineral and as such is usually
483 considered weak and incompetent in comparison to other minerals such as dolomite and quartz; rocks
484 with more weak and incompetent minerals would have lower bulk strengths and be less brittle than
485 those without, therefore we might expect lower fracture intensities in rocks containing more clay. This
486 relationship is observed elsewhere; Corbett et al. (1987) determine that chinks containing smectite
487 are weaker than those without because large clay masses act as soft inclusions that concentrate the
488 applied stress. Ferrill and Morris (2008) also suggest that clay rich carbonates are incompetent so they
489 are able to accommodate more pre-failure strain, resulting in lower fracture intensities at outcrop.
490 Both of these studies suggest the opposite relationship to what we observe from our data; we suggest
491 our observed positive correlation between fracture intensity and kaolinite content probably relates to
492 the fact that kaolinite-bearing rocks also tend to have significant proportions of quartz (Figure 10f),
493 which controls the bulk rock properties and resulting fracture intensity. Kaolinite percentages are very
494 low (<0.7 %) so probably do not have a significant impact on bulk rock properties; the correlation
495 between kaolinite content and estimated fracture intensity may be coincidental.

496 Our data suggests porosity and compositional factors are the main lithological controls on fracture
497 intensity, however there are several other studies that suggest other lithological properties influence
498 fracture intensity. Mechanical layer thickness is thought to correlate with fracture intensity; it is
499 thought that thicker beds will have wider spaced (and therefore lower intensity) fractures. Studies
500 find this relationship in carbonates (McQuillan, 1973; Huang & Angelier, 1989; Wennberg et al., 2006;
501 Wennberg et al., 2007; Barbier et al., 2012) and siliciclastics (Hobbs, 1967; Gross et al., 1995; Florez-
502 Niño et al., 2005). A limitation of our study area is that generally only the top surfaces of beds are
503 exposed so we cannot measure mechanical layer thickness to test this hypothesis. Another lithological
504 property that we have not been able to test is grain size, which has been seen to correlate with
505 fracture intensity in other field examples. Although we have backscatter electron images from our
506 hand specimens they only clearly show quartz grain boundaries; dolomite grain boundaries are very
507 difficult to identify, therefore we could not calculate average grain sizes for our hand specimens. Hanks
508 et al., 1997, suggest coarser grained rocks contain lower fracture intensities in carbonates. This would
509 fit our qualitative observations that lower fracture intensities are found in coarser grain-supported
510 dolomites on the Swift Reservoir Anticline. However, as Nelson (2001) points out, although a
511 increasing fracture intensity is often attributed to decreasing grain size, thinner beds often have lower
512 grain sizes so correlations between fracture intensity and grain size may actually relate to the
513 mechanical layer thickness.

514

515 **Conclusions**

516 Based on our data we suggest that the greatest controls on fracture intensity are porosity and quartz
517 content, followed by structural factors such as simple curvature and structural position. Where
518 lithology is constant (i.e. sampling at the same stratigraphic position along a transect) fracture
519 intensity has a positive correlation with fold simple curvature and bedding dip; the highest fracture
520 intensities are found in fold forelimb outcrops. Where variations in lithology occur (i.e. sampling
521 multiple bedding surfaces at different stratigraphic positions in the Castle Reef Formation), the
522 fracture intensity is unpredictable based on fold geometry; instead the fracture intensity is at least
523 partially controlled by porosity and quartz percentages that control the bulk rock strength and its
524 mechanical behaviour under stress. The implications of these results are that regions of a fold that
525 have undergone high stresses during folding, such as high curvature hinge zones and forelimbs that
526 may be preferentially be targeted during hydrocarbon exploration, may not necessarily provide well

527 connected fracture networks if the lithology is porous and quartz-poor. In this situation a better
528 fracture network may be found elsewhere in a region of lower curvature but higher quartz content
529 and lower porosity. Although structural factors influence fracture formation, it is the mechanical
530 properties of the rock that are the main control on fractured reservoir quality.

531

532 **Acknowledgements**

533 This research was funded by Oil Search Ltd, Santos Ltd and InterOil, through the University of
534 Aberdeen Fold-Thrust Research Group. Electron Microscopy was performed in the ACEMAC Facility at
535 the University of Aberdeen with assistance from John Still. Joyce Neilson is thanked for advice on the
536 use of ImageJ software. Midland Valley are thanked for the use of their Move software for field data
537 collection and model building. We thank Alfred Lacazette and Stefano Tavani for reviewing the
538 manuscript and providing constructive comments.

539 **References**

540 Barbier, M., Hamon, Y., Callot, J-P., Floquet, M. & Daniel, J-M., 2012. Sedimentary and diagenetic
541 controls on the multiscale fracturing pattern of a carbonate reservoir: The Madison Formation (Sheep
542 Mountain, Wyoming, USA). *Marine and Petroleum Geology*, 29, 50-67.

543 Batt, L. S. , Pope, M., Isaacson, P. E., Montañez, I., & Abplanalp, J., 2008. Upper Mississippian Antler
544 Foreland Basin Carbonate and Siliciclastic Rocks, East-Central Idaho and Southwestern Montana,
545 U.S.A.: Distinguishing Tectonic and Eustatic Controls on Deposition. *In* Controls on Carbonate
546 Platform and Reef Development. SEPM Special Publication 89, 147-170.

547 Bell, J. S., Price, P. R., & McLellan, P. J., 1994. In-situ Stress in the Western Canada Sedimentary
548 Basin. *In* G. Mossop and I. Shetsen, compilers, Geological Atlas of the Western Canada Sedimentary
549 Basin: Canadian Society of Petroleum Geologists and Alberta Research Council, Calgary and
550 Edmonton, 439-446.

551 Bell, J. S. & Babcock, E. A., 1986. The stress regime of the Western Canadian Basin and implications
552 for hydrocarbon production. *Bulletin of Canadian Petroleum Geology*, 34, 364-378.

553 Berg, R. B., 2002. Geologic Map of the Valier 30' X 60' Quadrangle, Northwestern Montana. Montana
554 Bureau of Mines and Geology Open File Report MBMG 453.

555 Bergbauer, S. & Pollard, D. D., 2004. A new conceptual fold-fracture model including prefolding joints,
556 based on Emigrant Gap anticline, Wyoming. *GSA Bulletin*, 116, 3-4, 294-307.

557 Chester, J. S., Logan, J. M. & Spang, J. H., 1991. Influence of layering and boundary conditions on fault-
558 bend and fault-propagation folding. *Geological Society of America Bulletin*, 103, 1059-1072.

559 Constenius, K. N., 1996. Late Paleogene extensional collapse of the Cordilleran foreland fold and
560 thrust belt. *Geological Society of America Bulletin*, 108, 20–39.

561 Cooper, M., 2007. Structural style and hydrocarbon prospectivity in fold and thrust belts a global
562 review. *In* Ries, A.C., Butler, R. W. H., & Graham, R. H. (eds), *Deformation of the Continental Crust: The
563 Legacy of Mike Coward*. Geological Society, London, Special Publications, 272, 447-472.

564 Corbett, K., Friedman, M. & Spang, J., 1987. Fracture Development and Mechanical Stratigraphy of
565 Austin Chalk, Texas. *AAPG Bulletin*, 71, 1, 17-28.

- 566 Cuong, T. X. & Warren, J. K., 2009. Bach Ho field, a fractured granitic basement reservoir, Cuu Long
567 Basin, offshore SE Vietnam: a 'buried-hill' play. *Journal of Petroleum Geology*, 32, 2, 129-156.
- 568 DeCelles, P. G., 2004. Late Jurassic to Eocene evolution of the Cordilleran Thrust Belt and foreland
569 basin system, Western U.S.A. *American Journal of Science*, 304, 105-168.
- 570 Dunne, D. E., LaFountain, L. J. & Jackson, R. E., 1973. Porosity Dependence and Mechanism of Brittle
571 Fracture in Sandstones. *Journal of Geophysical Research*, 78, 14, 2403-2417.
- 572 Engelder, T. & Lacazette, A., 1990. Natural hydraulic fracturing. In Barton, N. & Stephansson, O. (eds),
573 *Rock Joints: Proceedings of the international symposium on rock joints*. Loen, Norway. June 4-6, 1990:
574 A.A. Balkema, Brookfield.
- 575 Ferrill, D. A. & Morris, A. P., 2008. Fault zone deformation controlled by carbonate mechanical
576 stratigraphy, Balcones fault system, Texas. *AAPG Bulletin*, 92, 3, 359-380.
- 577 Fischer, M. P. & Jackson, P. B., 1999. Stratigraphic controls on deformation patterns in fault-related
578 folds: a detachment fold example from the Sierra Madre Oriental, northeast Mexico. *Journal of*
579 *Structural Geology*, 21, 613-633.
- 580 Florez-Niño, J-M., Aydin, A., Mavko, G., Antonellini, M. & Ayaviri, A., 2005. Fault and fracture systems
581 in a fold and thrust belt: An example from Bolivia. *AAPG Bulletin*, 89, 4, 471-493.
- 582 Fuentes, F., DeCelles, P. G., Constenius, K. N. & Gehrels, G. E., 2011. Evolution of the Cordilleran
583 foreland basin system in northwestern Montana, U.S.A. *GSA Bulletin*, 123, 3-4, 507-533.
- 584 Fuentes, F., DeCelles, P. G. & Constenius, K. N., 2012. Regional structure and kinematic history of the
585 Cordilleran fold-thrust belt in northwestern Montana, USA. *Geosphere*, 8, 5, 1104-1128.
- 586 Gross, M. R., Fischer, M. P., Engelder, T. & Greenfield, R. J., 1995. Factors controlling joint spacing in
587 interbedded sedimentary rocks: integrating numerical models with field observations from the
588 Monterey Formation, USA. In Ameen, M. S. (eds.), *Fractography: fracture topography as a tool in*
589 *fracture mechanics and stress analysis*. Geological Society, London, Special Publication, 92, 215-233.
- 590 Hanks, C. L., Lorenz, J., Teufel, L. & Krumhardt, A. P., 1997. Lithological and Structural Controls on
591 Natural Fracture Distribution and Behaviour Within the Lisburne Group, Northeastern Brooks Range
592 and North Slope Subsurface, Alaska. *AAPG Bulletin*, 81, 10, 1700-1720.
- 593 Hardebol, N. J., Callot, J. P., Bertotti, G. & Faure, J. L., 2009. Burial and temperature evolution in
594 thrust belt systems: Sedimentary and thrust sheet loading in the SE Canadian Cordillera. *Tectonics*,
595 28, TC3003, doi:10.1029/2008TC002335.
- 596 Harris, J. F., Taylor, G. L. & Walper, J. L., 1960. Relation of deformation structures in sedimentary rocks
597 to regional and local structure. *AAPG Bulletin*, 44, 1853-1873.
- 598 Hedlund, C. A. & Anastasio, D. J., 1994. Kinematics of fault-related folding in a duplex, Lost River Range,
599 Idaho, U.S.A. *Journal of Structural Geology*, 16, 4, 571-584.
- 600 Heidbach, O., Tingay, M., Barth, A., Reinecker, J., Kurfeß, D., & Müller, B.. The World Stress Map
601 database release 2008 doi:10.1594/GFZ.WSM.Rel2008.
- 602 Heidmann, J-C., Durand, J., Mallard, P., Ballard, J-F. & Moron, J-M., 2017. Discovery of a Bolivian
603 Foothills Giant Gas Field: Incahuasi. In Merrill, R. K. & Sternbach, C. A. (eds.), *Giant Fields of the Decade*
604 *2000-2010*, AAPG Memoir, 113, 153-164.

605 Hennings, P. H., Olson, J. E. & Thompson, L. B., 2000. Combining Outcrop Data and Three-Dimensional
606 Structural Models to Characterise Fractured Reservoirs: An Example from Wyoming. AAPG Bulletin,
607 84, 6, 830-849.

608 Hobbs, D. W., 1967. The Formation of Tension Joints in Sedimentary Rocks: An Explanation. Geological
609 Magazine, 104, 6, 550-556.

610 Holl, J. E. & Anastasio, D. J., 1992. Deformation of a foreland carbonate thrust system, Sawtooth
611 Range, Montana. GAS Bulletin, 104, 994-953.

612 Huang, Q. & Angelier, J., 1989. Fracture spacing and its relation to bed thickness. Geological Magazine,
613 126, 4, 355-362.

614 Hugman, R. H. H. & Friedman, M., 1979. Effects of Texture and Composition on Mechanical Behavior
615 of Experimentally Deformed Carbonate Rocks. AAPG Bulletin, 63, 9, 1478-1489.

616 Iñigo, J. F., Laubach, S. E. & Hooker, J. N., 2012. Fracture abundance and patterns in the Subandean
617 fold and thrust belt. Devonian Huamampampa Formation petroleum reservoirs and outcrops,
618 Argentina and Bolivia. Marine and Petroleum Geology, 35, 201-218.

619 Lacazette, A. & Engelder, T., 1992. Fluid-driven cyclic propagation of a joint in the Ithaca Siltstone,
620 Appalachian Basin, New York. In Evans, B. & Wong T.-F. (eds), Fault Mechanics and Transport
621 Properties of Rocks; a festschrift in honor of W. F. Brace: Academic Press, San Diego.

622 Lemiszki, P. J., Landes, J. D. & Hatcher Jr., R. D., 1994. Controls on hinge-parallel extension fracturing
623 in single-layer tangential-longitudinal strain folds. Journal of Geophysical Research, 99, B11, 22,027-
624 22,041.

625 Lisle, R. J., 1992. Constant bed-length folding: three-dimensional geometrical implications. Journal of
626 Structural Geology, 14, 2, 245-252.

627 Lisle, R. J., 1994. Detection of Zones of Abnormal Strains in Structures Using Gaussian Curvature
628 Analysis. AAPG Bulletin, 78, 12, 1811-1819.

629 Mauldon, M., Dunne, W. M. & Rohrbaugh Jr., M. B., 2001. Circular Scanlines and circular windows:
630 new tools for characterizing the geometry of fracture traces. Journal of Structural Geology, 23, 247-
631 258.

632 McMannis, W. J., 1965. Résumé of depositional and structural history of western Montana. Bulletin of
633 the American Association of Petroleum Geologists, 49, 11, 1801-1823.

634 McQuillan, H., 1973. Small-Scale Fracture Density in Asmari Formation of Southwest Iran and its
635 Relation to Bed Thickness and Structural Setting. AAPG Bulletin, 57, 12, 2367-2385.

636 Mitra, S., 1986. Duplex Structures and Imbricate Thrust Systems: Geometry, Structural Position, and
637 Hydrocarbon Potential. AAPG Bulletin, 70, 9, 1087-1112.

638 Mudge, M. R., 1982. A résumé of the structural geology of the Northern Disturbed Belt, northwest
639 Montana. Geological Studies of the Cordilleran Thrust Belt, 1, 91-122.

640 Mudge, M. R., Earhart, R. L., Whipple, J. W. & Harrison, J. E., 1982. Geological and Structure Map of
641 the Choteau 1° X 2° Quadrangle, Western Montana: U.S. Geological Survey Map, scale 1:250,000.

642 Mudge, M. R. & Earhart, R. L., 1983. Bedrock Geological Map of part of the Northern Disturbed Belt,
643 Lewis and Clark, Teton, Pondera, Glacier, Flathead, Cascade and Powell Counties, Montana: U.S.
644 Geological Survey Map, scale 1:125,000.

645 Nelson, R. A., 2001. Geological Analysis of Naturally Fractured Reservoirs, second ed. Gulf Publishing,
646 Houston, Texas.

647 Nichols, K. M., 1984. Stratigraphy of the upper part of the Madison Group, Sawtooth Range,
648 northwestern Montana. Montana Geological Society, 1984 Field Conference, Northwestern
649 Montana, p. 127 -14A.

650 Nichols, K.M., 1986. Regional significance of lithologic correlation of Mississippian rocks at Pentagon
651 Mountain and the Sawtooth Range, northwestern Montana, USGS Open-File Report 86-39 (one
652 Plate).

653 Odling, N. E., Gillespie, P., Bourguin, B., Castaing, C., Chilés, J-P., Christensen, N. P., Fillion, E., Genter,
654 A., Olsen, C., Thrane, L., Trice, R., Aarseth, E., Walsh, J. J. & Watterson, J., 1999. Variations in fracture
655 system geometry and their implications for fluid flow in fractured hydrocarbon reserves. Petroleum
656 Geoscience, 5, 373-384.

657 Ortega, O. J., Gale, J. F. W. & Marrett, R., 2010. Quantifying diagenetic and stratigraphic controls on
658 fracture intensity in platform carbonates: An example from the Sierra Madre Oriental, northeast
659 Mexico. Journal of Structural Geology, 32, 1943-1959.

660 Price, N.J., 1966. Fault and Joint Development in Brittle and Semi-brittle Rocks (Pergamon, Oxford).

661 Price, R.A., 1994. Cordilleran tectonics and the evolution of the Western Canada Sedimentary Basin.
662 *In* G. Mossop & I. Shetsen, compilers, Geological Atlas of the Western Canada Sedimentary Basin:
663 Canadian Society of Petroleum Geologists and Alberta Research Council, Calgary and Edmonton, 13–
664 24.

665 Ramsay, J. G., 1967. Folding and Fracturing of Rocks. McGraw-Hill, New York.

666 Reid, S.K. & Dorobek, S., 1993. Sequence stratigraphy and evolution of a progradational, foreland
667 carbonate ramp, Lower Mississippian Mission Canyon Formation and stratigraphic equivalents,
668 Montana and Idaho. *In* Carbonate sequence stratigraphy: recent developments and applications.
669 AAPG Memoir, 57, 327-352.

670 Rohrbaugh, M. B., Dunne, W. M. & Mauldon, M., 2002. Estimating fracture trace intensity, density,
671 and mean length using circular scan lines and windows. AAPG Bulletin, 86, 12, 2089-2104.

672 Ross, D.L., 2016. Structural Geology of the North-Half of the Swift Reservoir Culmination, Sawtooth
673 Range, Montana. MSc Thesis, Montana State University, Bozeman, Montana, 134p, 2 plates.

674 Salvini, F. & Storti, F., 2001. The distribution of deformation in parallel fault-related folds with
675 migrating axial surfaces: comparison between fault-propagation and fault-bend folding. Journal of
676 Structural Geology, 23, 25-32.

677 Singdahlsen, D. S., 1986. Structural geology of the Swift Reservoir Culmination, Sawtooth Range,
678 Montana. MSc Thesis, Montana State University, Bozeman, Montana, 124 p., 2 plates.

679 Tavani, S., Storti, F., Lacombe, O., Corradetti, A., Muñoz, J. A. & Mazzoli, S., 2015. A review of
680 deformation pattern templates in foreland basin systems and fold-and-thrust belts: Implications for
681 the state of stress in the frontal regions of thrust wedges. Earth-Science Reviews, 141, 82-104.

- 682 Ward, E. M. G., 2007. Development of the Rocky Mountain Foreland Basin: Combined Structural,
683 Mineralogical, and Geochemical Analysis of Basin Evolution, Rocky Mountain Thrust Front, Northwest
684 Montana. Ph.D thesis, Missoula, University of Montana.
- 685 Ward, E. M. G. & Sears, J. W., 2007. Reinterpretation of fractures at Swift Reservoir, Rocky Mountain
686 thrust front, Montana Passage of a Jurassic forebulge? In Sears, J. W., Harms, T. A. & Evenchick, C. A.
687 (eds.) Whence the Mountains? Inquiries into the Evolution of Orogenic Systems: A Volume in Honor
688 of Raymond A. Price: Geological Society of America Special Paper 433, 197-210.
- 689 Watkins, H., Bond, C. E., Healy, D. & Butler, R. W. H., 2015a. Appraisal of fracture sampling methods
690 and a new workflow to characterise heterogeneous fracture networks at outcrop. *Journal of Structural*
691 *Geology*, 72, 67-82.
- 692 Watkins, H., Butler, R. W. H., Bond, C. & Healy, D., 2015b. Influence of structural position on fracture
693 networks in the Torridon Group, Achnashellach fold and thrust belt, NW Scotland. *Journal of Structural*
694 *Geology*, 74, 64-80.
- 695 Watkins, H., Healy, D., Bond, C. E. & Butler, R. W. H., 2018. Implications of heterogeneous fracture
696 distribution on reservoir quality; an analogue from the Torridon Group sandstone, Moine Thrust Belt,
697 NW Scotland. *Journal of Structural Geology*, 108, 180-197.
- 698 Wennberg, O. P., Svånå, T., Azizzadeh, M., Aqrabi, A. A. M., Brockbank, P., Lyslo, K. B. & Ogilvie, S.,
699 2006. Fracture intensity vs. mechanical strain in platform top carbonates: the Aquitanian of the
700 Asmari Formation, Khaviz Anticline, Zagros, SW Iran. *Petroleum Geoscience*, 12, 235-246.
- 701 Wennberg, O. P., Azizzadeh, M., Aqrabi, A. A. M., Blanc, E., Brockbank, P., Lyslo, K. B., Pickard, N.,
702 Salem, L. D. & Svånå, T., 2007. The Khaviz Anticline: an outcrop analogue to giant fractured Asmari
703 Formation reservoirs in SW Iran. In Lonergan, L., Jolly, R. J. H., Rawnsley, K. & Sanderson, D. J. (eds.)
704 *Fractured Reservoirs*, Geological Society, London, Special Publications, 270, 23-42.

705

706 **Figure captions**

707 *Figure 1: Simplified geological map of the Sawtooth Range and surrounding area. Extent of Figure 3a*
708 *is shown by the black box. Adapted from Mudge et al., 1982; Mudge & Earhart, 1983.*

709 *Figure 2: a) Sedimentary log through the fold forelimb on the southern side of the Swift Reservoir dam*
710 *cut. Bed thickness here decreases with decreasing grain size. b) Field photograph of the southern side*
711 *of the dam cut showing the location of the sedimentary log (Figure 2a). Three lithological units are*
712 *identified: mudstone, wackestone-packstone, grainstone. The majority of fracture sampling sites are*
713 *located higher in the stratigraphy than the log, for example on the mudstone outcrops at the top of*
714 *the image. c) An example of a fractured mudstone (MSD) bedding surface. d) An example of a fractured*
715 *grainstone (GSD) bedding surface.*

716 *Figure 3: a) Geological map of Swift Reservoir and surrounding region showing the location of the Swift*
717 *Reservoir Anticline (SRA) and line of section (Figure 3d) adapted from Mudge & Earhart, 1983. b) 3D*
718 *photogrammetric model of the Swift Reservoir Anticline showing its asymmetric structure. c) key to*
719 *geological map and cross section (Figure 3a, Figure 3d). d) Cross section through the Swift Reservoir*
720 *Anticline showing the local structural style. MSBT, Major Steel Backbone Thrust; ST, Swift Thrust; SRA,*
721 *Swift Reservoir Anticline; ECIZ, Eagle Creek Imbricate Zone; IZ, Eagle Creek Imbricate Zone in the*
722 *subsurface; FLT, Fish Lake Thrust; OMT, Old Man Thrust; MLT, Mitten Lake Thrust; BT12-1, Blackfeet*
723 *Tribal 12-1 well; W-1, Wickware 1. e) Schematic restoration of the Swift Reservoir Anticline showing*

724 an asymmetric anticline with a steep forelimb that could result from fault propagation folding or
725 trishear or the combination of both. The solid red line shows the extent of the thrust at this
726 development stage and the dashed red line shows where the thrust will subsequently cut through the
727 fold to emplace the fold to its current location.

728 Figure 4: Aerial photograph (from Google Earth) showing the locations of sampling sites and cross
729 sections (T1-T11) used to construct the 3D model (Figure 5). The size of the circles at each sampling
730 site reflect the magnitude of fracture intensity, and the colour of the circle reflects the lithology at each
731 sampling site. Transect/cross section locations are shown by orange lines; the fold hinge is shown by
732 the green line; structural zone (forelimb, hinge zone, backlimb) boundaries are shown by yellow lines.

733 Figure 5: 3D model of the top Castle Reef Formation constructed from parallel cross sections colour-
734 mapped for simple curvature. The positions of cross sections/field transects (T1-T11) are shown as
735 orange lines.

736 Figure 6: a) scatter graph of fracture intensity versus fold simple curvature (extracted from the 3D
737 model-Figure 5), showing a positive correlation for MSD sites, and almost no correlation for MGSD and
738 GSD sites. b) scatter graph of fracture intensity versus bedding dip, showing a positive correlation for
739 MSD sites and negative correlations for MGSD and GSD sites. c) Bar chart showing the average fracture
740 intensity for MSD, MGSD and GSD sampling sites in different structural positions. For all graphs blue
741 datapoints are from Mud-Supported Dolomites (MSD), yellow are from an intermediate phase (MGSD)
742 and red are from Grain-Supported Dolomites (GSD).

743 Figure 7: a) Scatter graph of fracture intensity versus fold simple curvature (extracted from the 3D
744 model-Figure 5) for transect 1 sampling sites. b) Scatter graph of fracture intensity versus bedding dip
745 for transect 1 sampling sites. c) Cross section through transect 1 showing the change in fracture
746 intensity with structural position. d) Scatter graph of fracture intensity versus fold simple curvature
747 (extracted from the 3D model-Figure 5) for transect 10 sampling sites. e) Scatter graph of fracture
748 intensity versus bedding dip for transect 10 sampling sites. f) Cross section through transect 10 showing
749 the change in fracture intensity with structural position. g) Key to cross sections. See Figures 4 & 5 for
750 transect locations. For all figures blue data points are from Mud-Supported Dolomites (MSD), yellow
751 are from an intermediate phase (MGSD) and red are from Grain-Supported Dolomites (GSD).

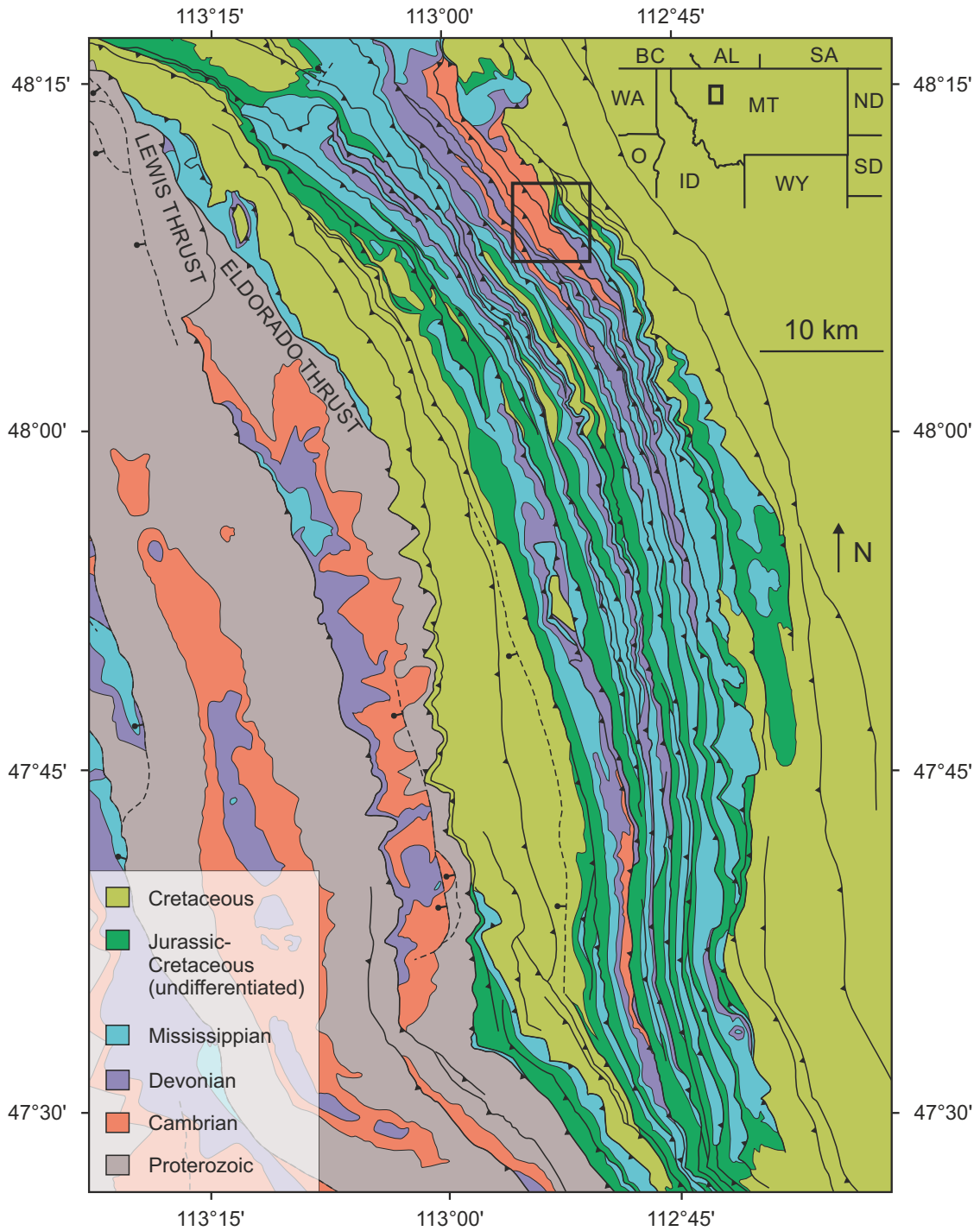
752 Figure 8: a) Scatter graph showing fracture intensity distribution in GSD, MGSD and MSD lithologies.
753 Box and whisker plots for each lithology show the minimum, maximum, first quartile, third quartile
754 and median. b) Bar chart showing the average fracture intensity for each lithology observed in the
755 field. Fracture intensity decreases from mud-supported to grain-supported dolomites.

756 Figure 9: a) Binary image showing the porosity distribution (black) for Figure 9e; porosity for this image
757 is 32.51%. b) Binary image showing the calcite distribution (black) for Figure 9e; calcite percentage for
758 this image is 1.90%. c) Binary image showing the quartz distribution (black) for Figure 9e; quartz
759 percentage for this image is 1.51%. d-g) Representative BSE (Back-Scatter Electron) images showing
760 GSD (d-e) and MSD (f-g) lithologies. h) Average composition for GSD (red) and MSD (blue) hand
761 specimens.

762 Figure 10: scatter graphs for fracture intensity versus a) porosity percentage, b) dolomite percentage,
763 c) quartz percentage, d) kaolinite percentage, e) calcite percentage. f) Scatter graph for quartz
764 percentage versus kaolinite percentage. Moderate correlations are seen between fracture intensity
765 and porosity, quartz content and kaolinite content. Fracture intensity has a weak correlation with
766 dolomite content and calcite content. A positive correlation between quartz percentage and kaolinite
767 percentage is observed.

768 *Figure 11: Schematic model of fracture intensity variation on the Swift Reservoir Anticline; fracture*
769 *intensity increases with increasing fold curvature in a given lithology. Fracture intensity is much lower*
770 *in grain-supported dolomites with higher percentages of quartz and porosity than mud-supported*
771 *dolomites, regardless of fold curvature and structural position.*

FIGURE 1



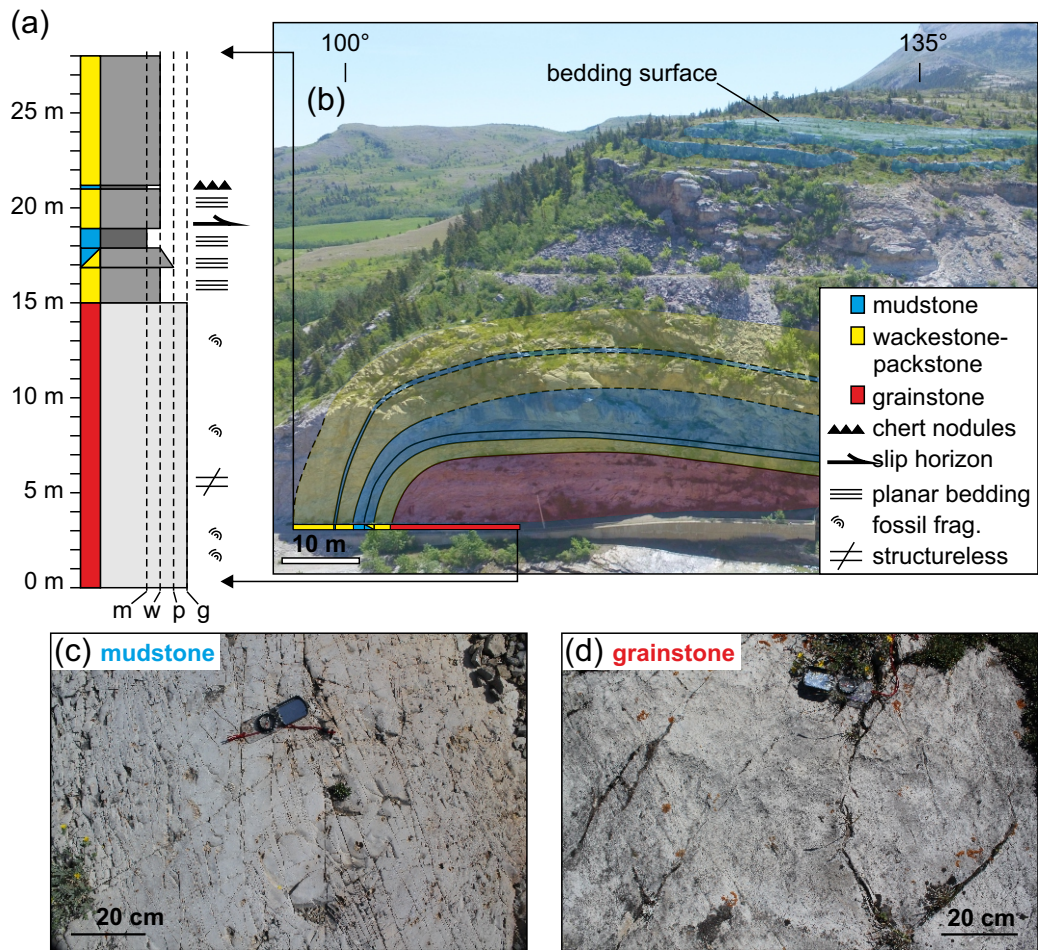


FIGURE 2

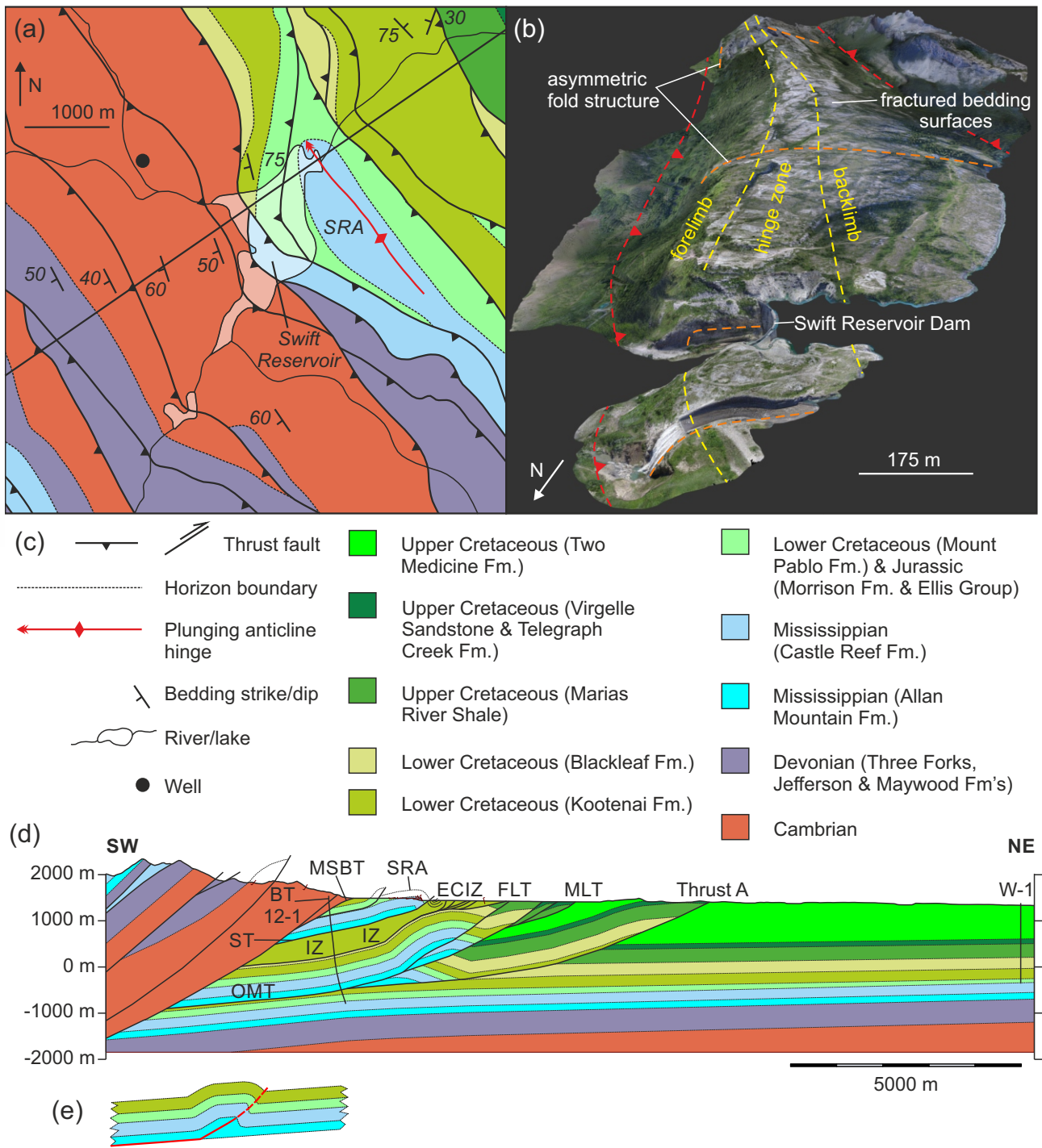


FIGURE 3

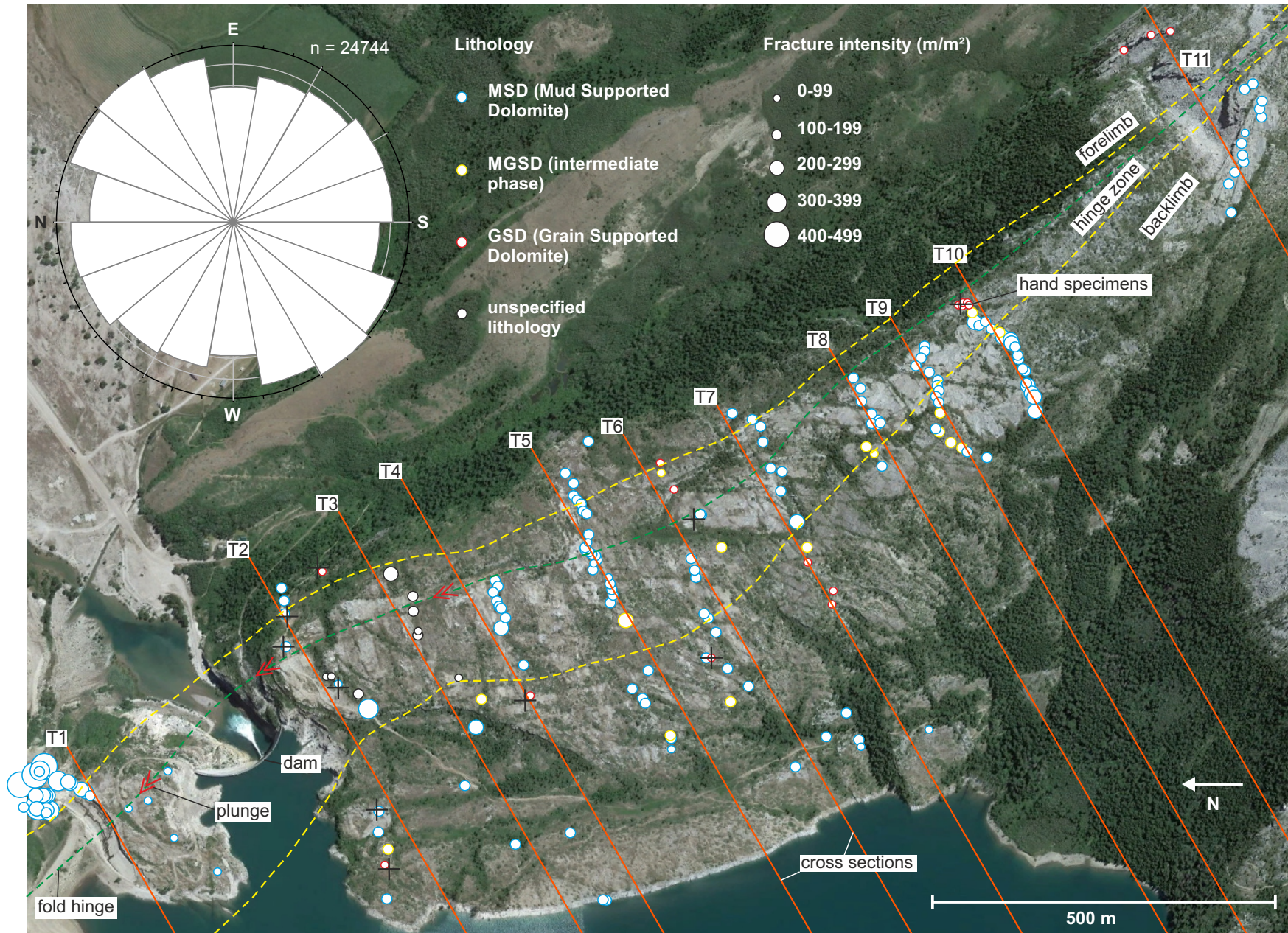


FIGURE 4

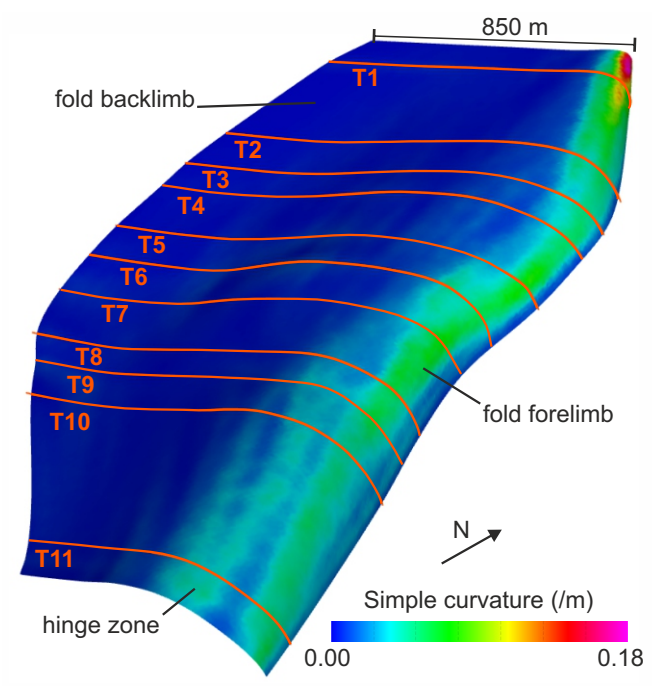


FIGURE 5

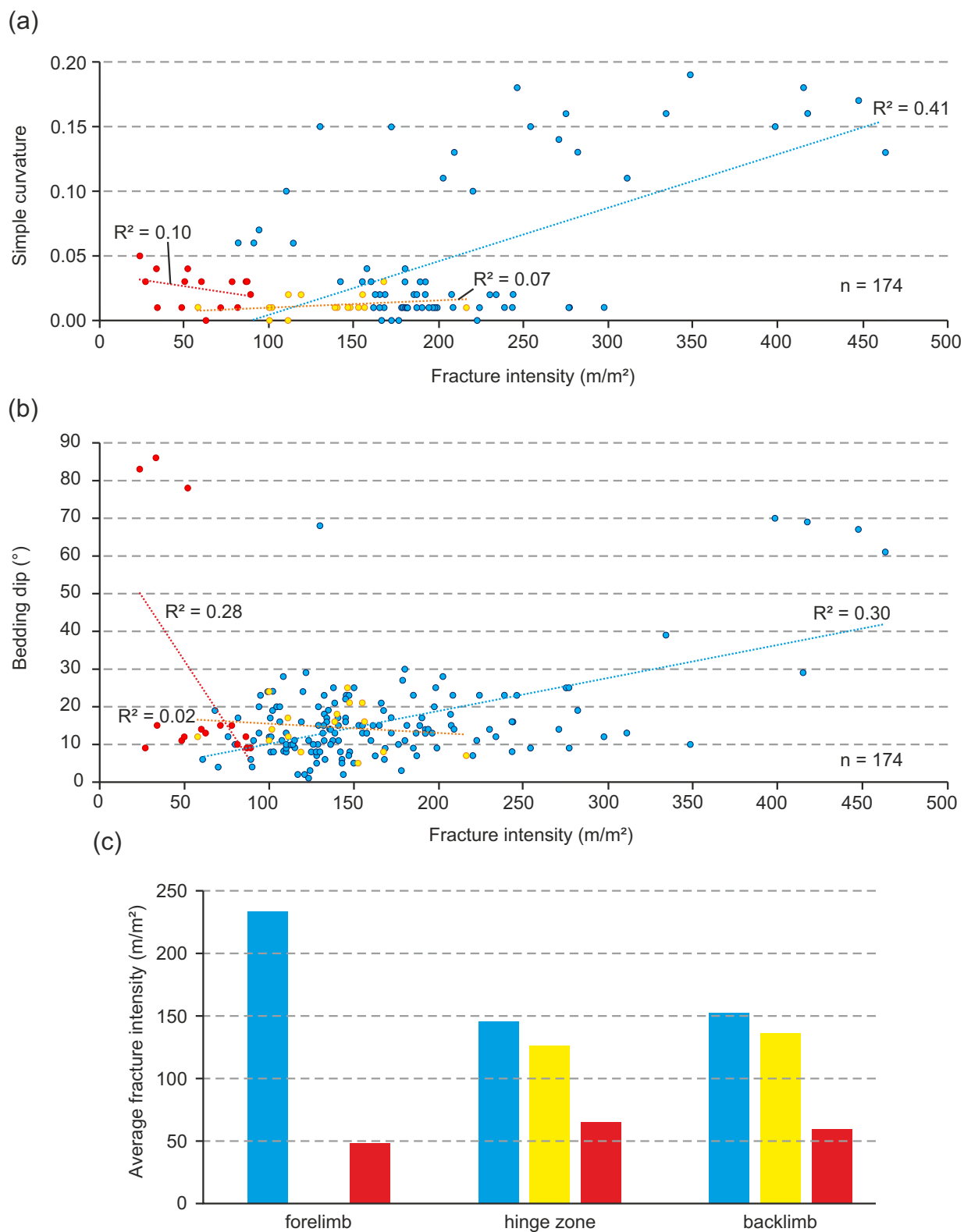
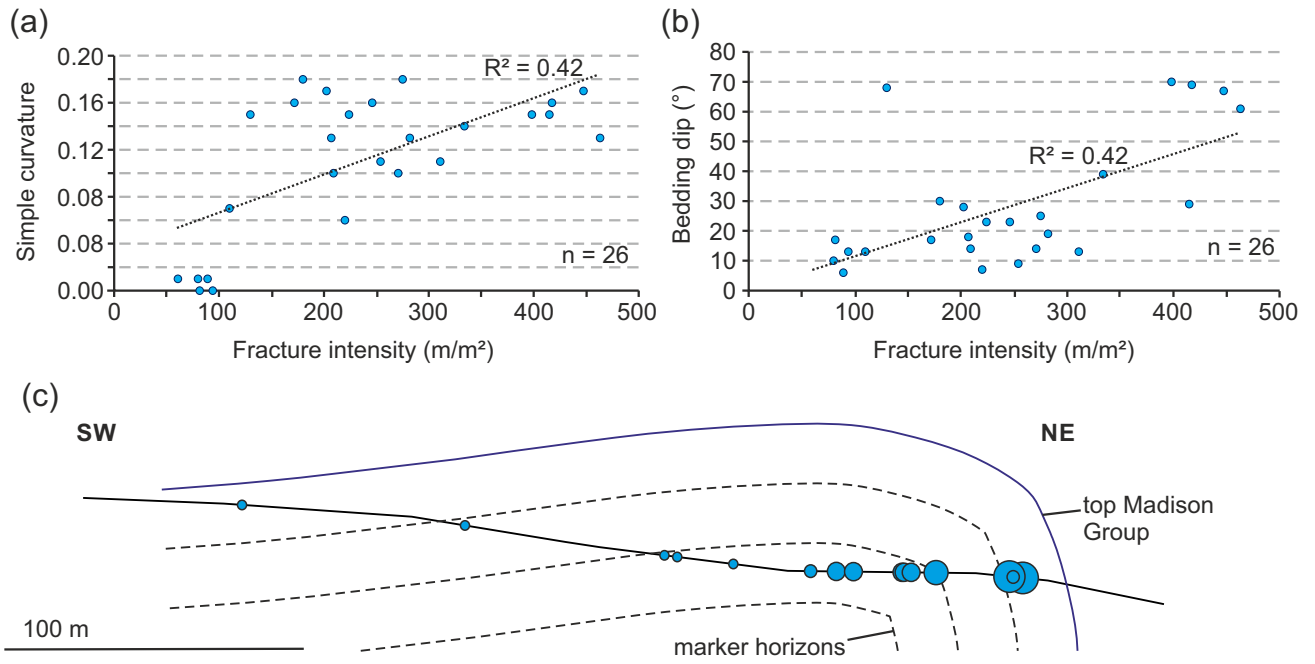


FIGURE 6

Transect 1



Transect 10

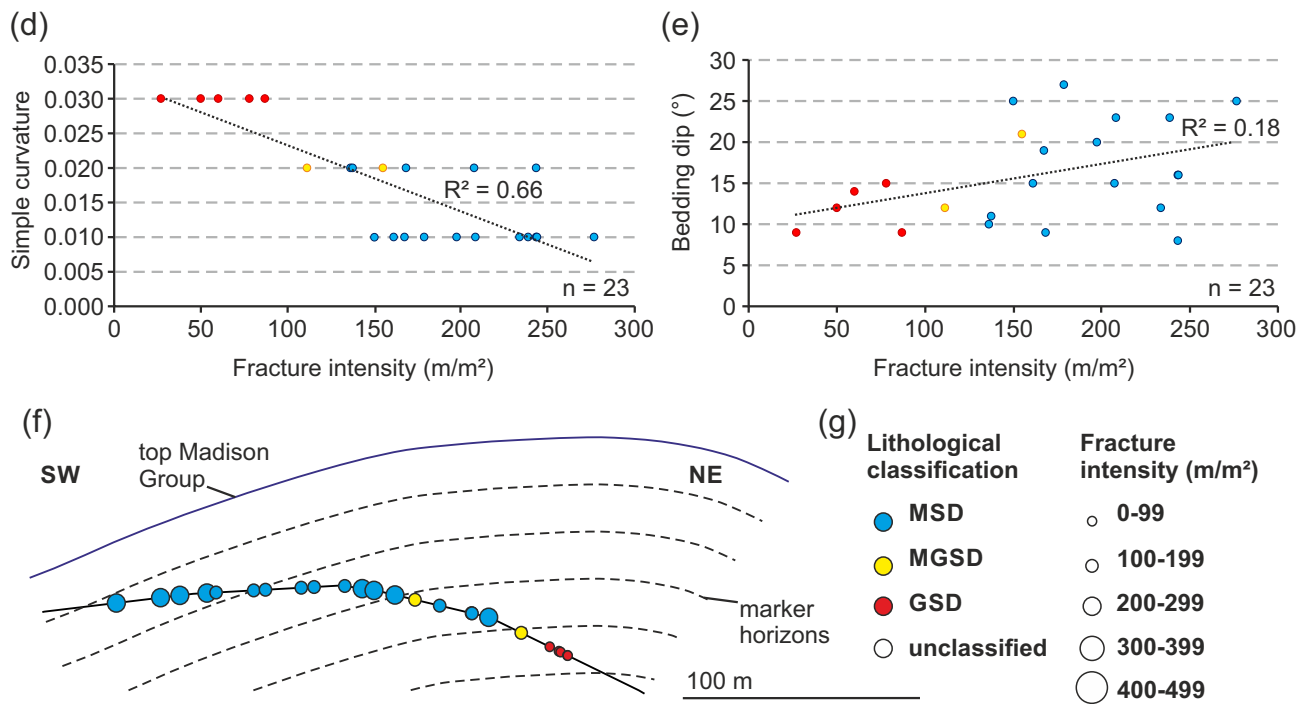


FIGURE 7

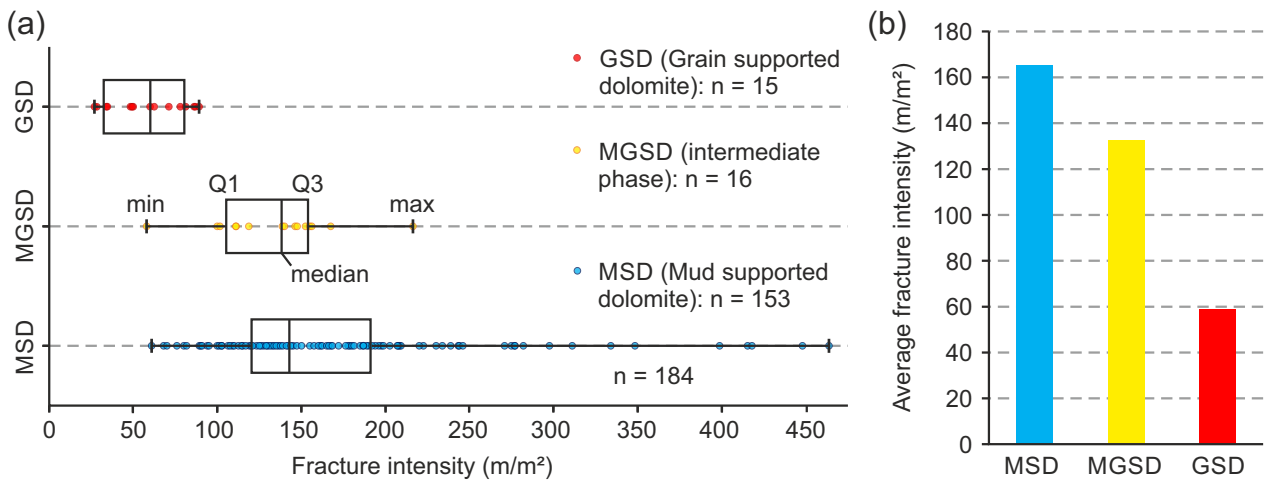


FIGURE 8

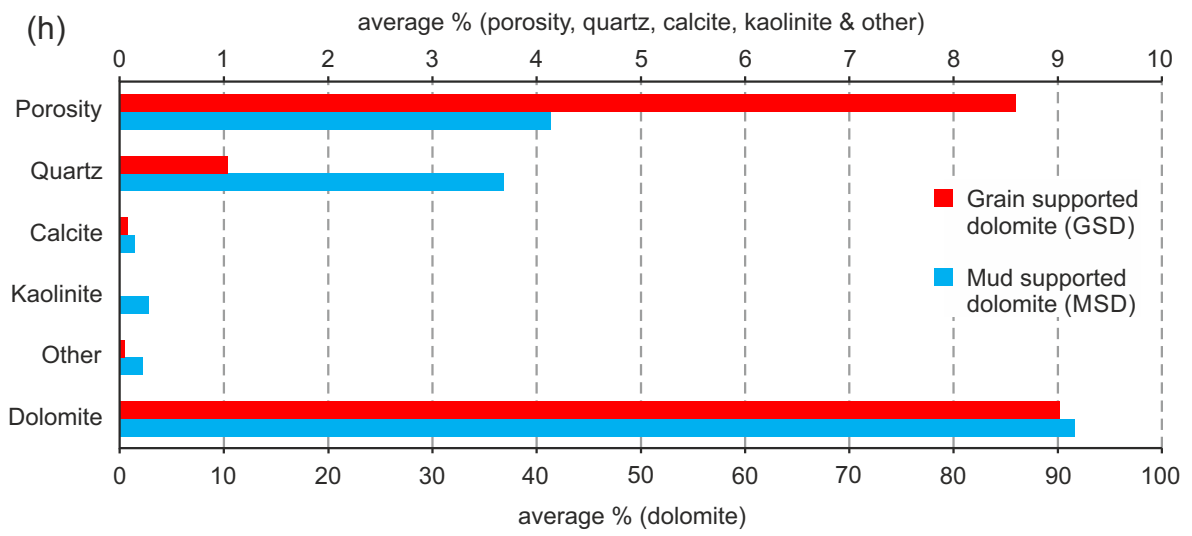
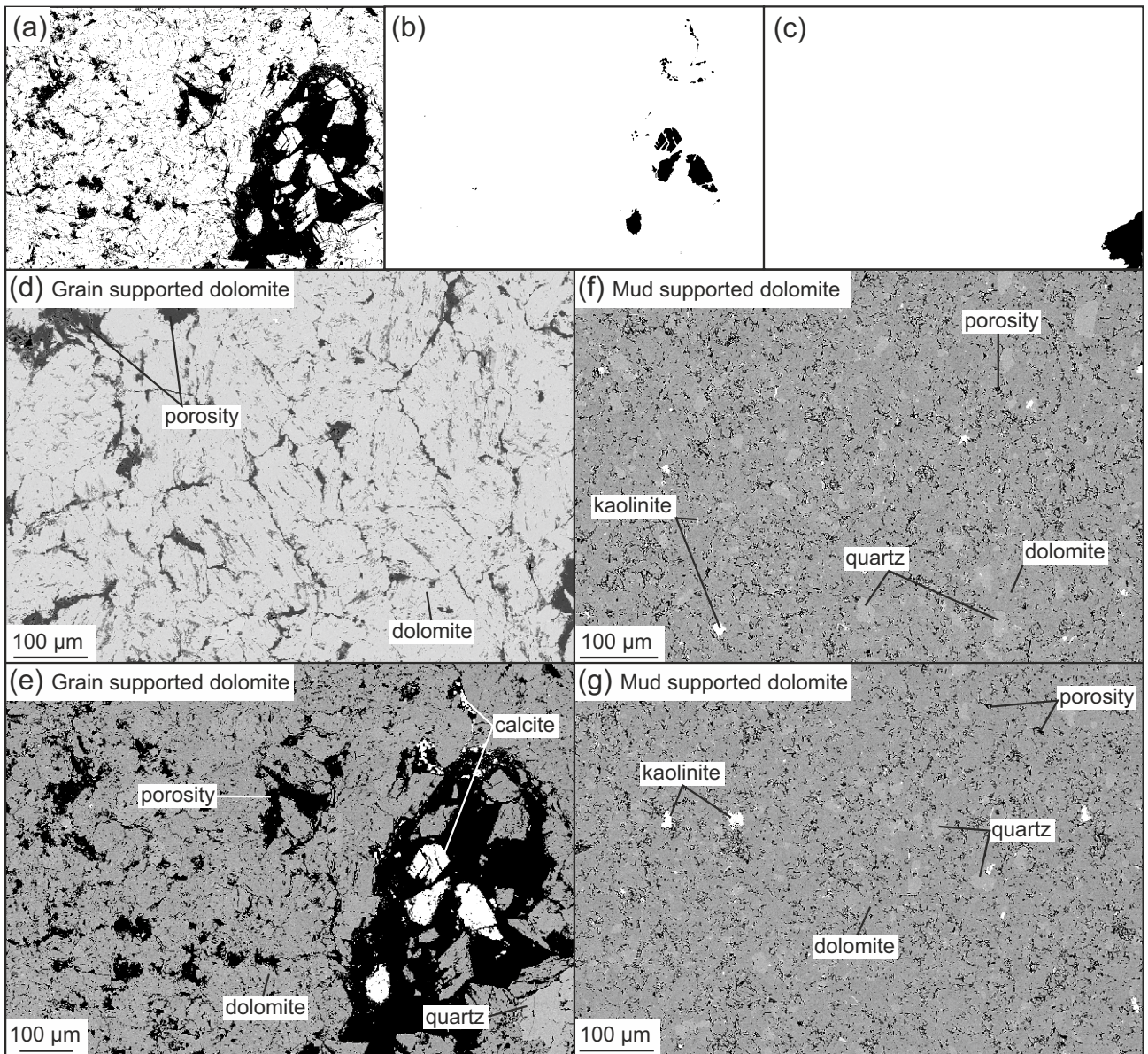


FIGURE 9

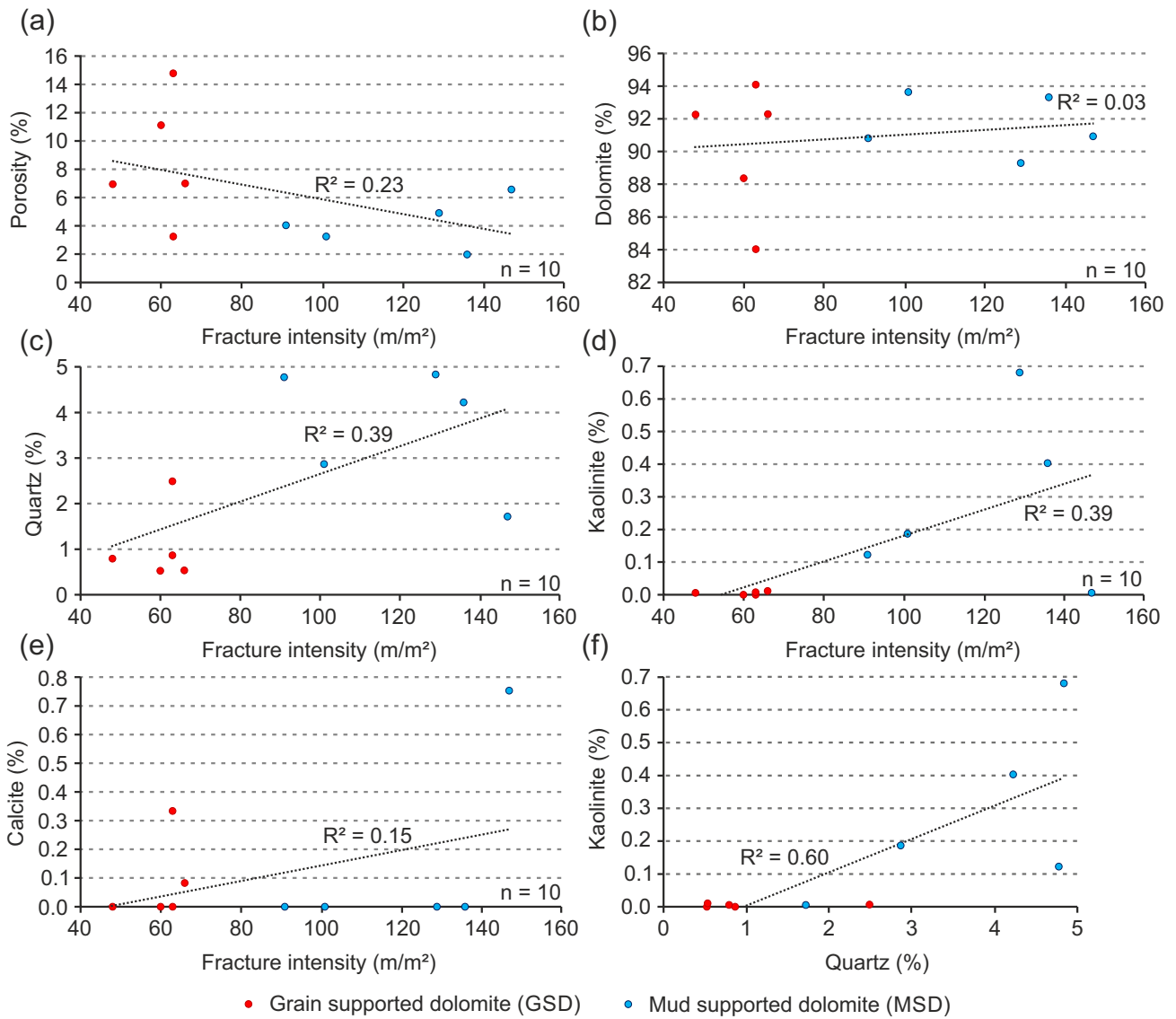


FIGURE 10

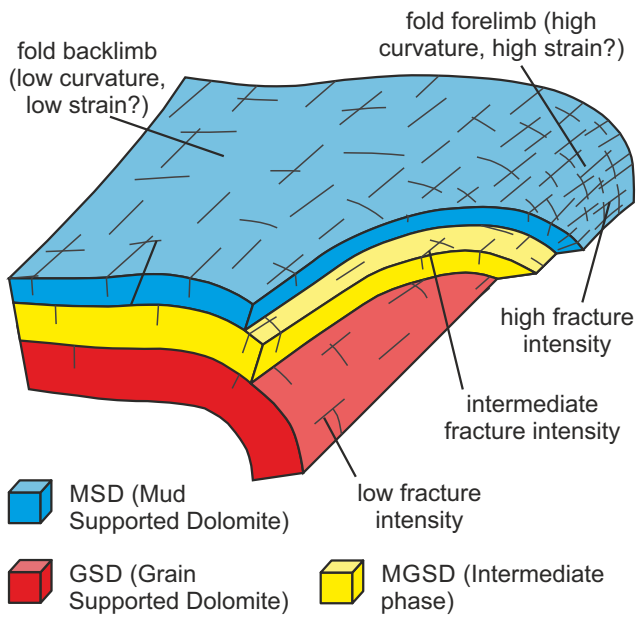


FIGURE 11